
Article:
Deng, F. and Qin, N. (2018) Quantitative comparison of 2D and 3D shock control bumps for drag reduction on transonic wings. Proceedings of the Institution of Mechanical Engineers, Part G: Journal of Aerospace Engineering, 233 (7). pp. 2344-2359. ISSN: 0954-4100

https://doi.org/10.1177/0954410018778815

Quantitative Comparison of 2D and 3D Shock Control Bumps for Drag Reduction on Transonic Wings

Feng Deng[1]
Key Laboratory of Advanced Design Technology of Flight Vehicle, Nanjing University of Aeronautics and Astronautics, Nanjing 210016, China

Ning Qin[2]
Department of Mechanical Engineering, University of Sheffield, Sheffield S1 3JD, UK

In this paper, the design spaces of the 2D and 3D shock control bumps on an infinite unswept natural laminar flow wing are investigated by adopting an optimization enhanced parametric study method. The design space spanned by the design variables are explored through a series of design optimization and their landscapes around the optima are revealed. The effects of the bump spacing, bump length and Mach number are investigated respectively around the optima. The maximum cross-sectional area, bump incident angle and aspect ratio are found to be important design parameters. The associated flow physics is discussed in relation to these parameters. The comparative performance of the 2D and 3D bumps are explained in the context of the transonic area rule. Two types of flow separation are identified by varying the bump aspect ratio at off-design conditions. It is concluded that the 2D and 3D shock control bumps can have nearly the same performances at optimal designs with similar cross-sectional areas. Some practical design principles and guidelines are suggested.

Nomenclature

C_L = lift coefficient

C_D = drag coefficient

Cp = pressure coefficient

S_{mc} = maximum cross-sectional area

c = chord length

[1] University Lecturer, Department of Aircraft Design, corresponding author, fdeng@nuaa.edu.cn.
[2] Professor of Aerodynamics, Department of Mechanical Engineering.

α = angle of attack

θ = bump incident angle

λ = bump aspect ratio

I. Introduction

According to the Breguet Range Equation, there are two possible ways to improve the aerodynamic efficiency of a civil transport aircraft. One is to maximize the lift-drag ratio and the other is to increase the flight velocity. However, they conflict with each other when the flight velocity of the aircraft approaches the speed of sound due to the appearance of shock waves. In recent years, shock control bumps had been proposed to relieve the detrimental effects of the shock waves and potentially this shock control technique will be applied to the next generation civil transport aircraft flying at high transonic speeds.

The concept of 2D shock control bump was first introduced in the literature. The earliest shock control method by changing surface curvature can be traced back to Tai's work in the late 1970s [1]. It was found that theoretically the drag-divergence Mach number could be increased by carefully adding a single "hump" on the upper surface of a supercritical airfoil. Later this finding was further confirmed by experiments [2]. In the early 1990s, Ashill and Fulker [3, 4] proposed to utilize local 2D bumps to reduce the strength of the normal shock waves on laminar flow airfoils. Since then the potential of 2D shock control bumps has been investigated by a number of computational and experimental studies [5-9]. Some comprehensive investigation has been carried out by two European projects, EUROSHOCK I [5] and EUROSHOCK II [8]. The studies have shown that local contour bumps are the most efficient shock control devices if drag reduction is considered as the primary design objective. The shortcomings of 2D bumps were confirmed in their research with poor off-design performance. To improve the robustness of shock control bumps, Stanewsky [7] suggested that deformable bumps or adaptive bumps should be adopted, but at the cost of an increase of structure weight and complexity.

To unleash the possibility of robust shock control bumps and for convenient distribution over 3D wings, 3D shock control bumps were proposed and investigated by Qin *et al.* [10] and their advantage in comparison to the 2D bump in design robustness was highlighted [11]. By allowing geometric variation in the span-wise direction, it is possible to further improve the performance of shock control bumps. Later a combined research between Qin [11-13] and Babinsky [14, 15] has shown that 3D bumps can achieve the same level of drag reduction as 2D bumps and

are more robust in some cases. It is obvious that 3D bumps can be more easily integrated into the structure of the wing and more easily deformed actively due to their geometrical compactness, considering the potential development of adaptive bumps. Furthermore, 3D bumps also provide the possibility to generate streamwise vortices [15-17], which are beneficial for improving the off-design performances, such as buffet alleviation, investigated by Eastwood and Jarrett [18]. Recently, Jones *et al.* [19] investigated the effects of swept flows for 3D bumps, and a new geometric parameter, termed bump orientation, was found to be crucial to the performance under swept flows. Hinchliffe and Qin [20] achieved significant drag reduction by placing 3D bumps in the sensitivity regions on the M6 wing upper surface. Recent research on 3D shock control bumps was well summarized by Bruce and Colliss [21].

Since the beginning of the 3D bump investigation, some distinct features are identified by numerous researchers. For 2D bumps, a normal shock wave can be turned into a series of compression waves for a contoured bump or a λ-structured shock wave for a ramp bump, reducing entropy increase in both cases. Ideally, the former can lead to an isentropic compression in place of a shock wave with total elimination of the wave drag. For a 3D bump, researchers have also observed similar wave structures along its center axis both in the experiments and simulations, and these structures will decay in the spanwise direction due to the reduction of local effective bump. One interesting finding reported by Ogawa *et al.* [15] is that this decay is actually quite slow and the 3D controlled wave structure covers a much larger area than the actual 3D bump geometry. Another discovery made by Qin *et al.* [11] is that the optimized 3D bumps tend to be much higher than the optimized 2D bumps at the same conditions.

However, there are still some remaining unsolved problems regarding the understanding of the flow physics for shock control bumps. One of these is why an optimized 3D bump performs similarly with an optimized 2D bump. Bruce and Colliss [21] argued that the reason is that an array of spanwise spaced discrete 3D bumps can produce a quasi-2D shock structure due to the overlap of flow structures of adjacent 3D bumps. However, in the numerical simulations by Qin *et al.* [11] and König *et al.* [22], it is obvious that the flow fields exhibit strong three-dimensional structures in terms of surface pressure distributions, although the spanwise wave patterns do exhibit some similarity. After reviewing numerous research works focusing on the comparison of 2D and 3D bumps, Bruce and Colliss [21] pointed out that the relation between 2D and 3D bumps was still unclear.

In this work, an optimization enhanced parametric study method has been developed to explore the design spaces for both 2D and 3D contour bumps on an infinite unswept natural laminar flow wing. It is believed that the

interaction of the design variables can be properly investigated by this novel parametric study method so that more flow physics can be unraveled to help understand the aerodynamic performance of shock control bumps. The detailed quantitative relationship between 2D and 3D bumps will be established and the effects of key shock control parameters will be investigated in detail.

The paper first describes the methods used for analyses, including the parameterization methods of shock control bumps and the optimization enhanced parametric study method. Then the validation of the CFD solver is presented. Finally, the effects of shock control parameters are examined and the flow mechanisms of both 2D and 3D bumps are discussed, before the paper is concluded.

II. Methods

A. Parameterization of 2D and 3D bumps

In this study, the bumps are added on the top of a given wing surface and the bump function represents the difference between the datum wing surface and the bump surface. Following the work of Qin *et al.* [11], a 2D contour bump is designed by four parameters, as illustrated in Figure 1a, which are bump length (*L*), bump crest position (x_{crest}), relative crest position (*R*) and bump height (*H*). Two different third order polynomials are used to represent the shape of a 2D bump, let them be $y_1(x)$ and $y_2(x)$, respectively. Then, the equations for a 2D bump can be defined as

$$y_1(x_{start}) = y_2(x_{end}) = 0 \tag{1a}$$

$$y_1'(x_{start}) = y_2'(x_{end}) = 0 \tag{1b}$$

$$y_1(x_{crest}) = y_2(x_{crest}) = H \tag{1c}$$

$$y_1'(x_{crest}) = y_2'(x_{crest}) = 0 \tag{1d}$$

where $x_{start} = x_{crest} - L \times R$ is the starting point of the bump and $x_{end} = x_{start} + L$ is the end point of the bump. The gradients at the starting point and end point are both set to zero to enforce a tangential condition (C^1) at the intersection points between the bump geometry and the original wing.

To be consistent with the 2D bump, a 3D bump is generated by gradually decreasing the height of a 2D bump along its span-wise direction, and the variation is also represented by a third order polynomial, let it be $y_3(x, z)$. It is to make sure that the streamwise cross-sectional area distribution of a 3D bump is exactly the same as that of a 2D bump if the following conditions are satisfied: a) the maximum cross-sectional area of this 3D bump is equal to that of this 2D bump; b) the bump length, bump crest position and relative crest position of them are the same.

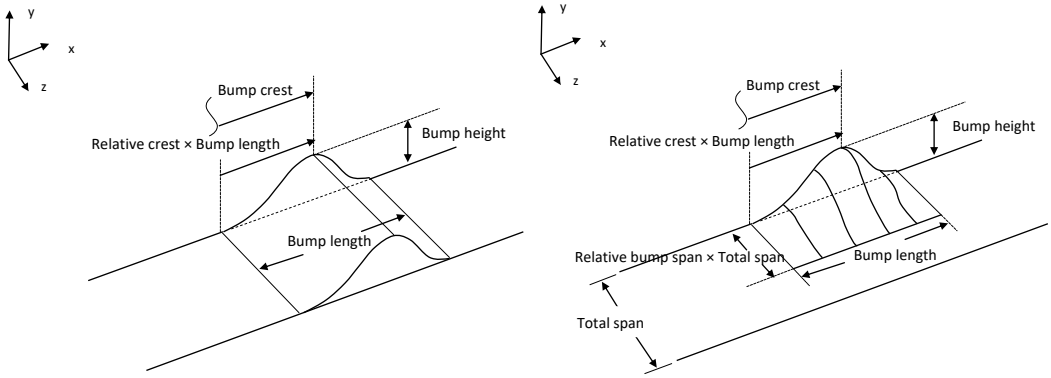

a) 2D bump b) Half of a 3D bump

Fig. 1 Parameterization of shock control bumps.

Figure 1b shows a schematic of the parameters for half of a 3D bump. It can be seen that there are two additional spanwise parameters for a 3D bump. The first one is the total span (*TS*), which determines the number of 3D bumps per unit wing span, and the second one is the relative bump span (*RS*), which controls the effective bump width. The equations for a 3D bump in the chordwise direction are the same as that of a 2D bump as shown in equation (1), except that the *H* in equation (1c) should be replaced by $y_3(x, z)$, which must satisfy the following equations:

$$y_3(x, z_{crest}) = H \tag{2a}$$

$$y_3'(x, z_{crest}) = 0 \tag{2b}$$

$$y_3(x, z_{end}) = 0 \tag{2c}$$

$$y_3'(x, z_{end}) = 0 \tag{2d}$$

where z_{crest} is the maximum crest of the bump and $z_{end} = z_{crest} + TS \times RS$.

B. Optimization enhanced parametric study method

If there are only a few design variables or the functional calculation is cheap, the grid sampling method is often used to fully understand the structure of a design space. However, because of the curse of dimensionality, it is difficult to apply the grid sampling method directly to explore a high-dimensional design space while the functional calculation is expensive, such as the case for RANS solutions. Therefore a simplified grid sampling method, also known as a parametric study, was favored by most of the researchers. The procedure of this parametric study can be briefly described as following: firstly, allow one design variable to vary while the other design variables are kept constant; then let the second design variable vary, and so on. However, since this simplified method only allows one design variable to vary at one time, the conclusions based on this may be misleading as it does not account for the interaction of the various design parameters.

In this research, an optimization enhanced parametric study method is developed. The principle of this method is described here. Firstly, a one-dimensional grid sampling method is applied to a chosen design variable. Then, at each grid point, an optimization is completed with the other design variables as free ones. By allowing the other variables to change at each grid point, the objective function can be always at the optimum for a specified variable being studied.

The motivation is that the most important part of a design space is usually the area around the optimum. Then the area in a design space with no importance can be skipped to make the exploration affordable. This allows the behavior of the chosen parameter to be properly investigated in the design space while the other design variables are at their optimum, allowing extraction of flow physics and design robustness from the optimized design in relation to the chosen parameter.

Let m be the number of grid sampling points for a specified variable from k design parameters. Assume the number of functional calculations needed by optimization is n with k-1 design variables. Then the total number of functional calculations required is equal to $n \times m$ for the exploration of this chosen design variable.

As can be seen, to explore the design space, the computation is much more demanding than a straightforward optimization problem. It requires a large number of optimizations in relation to chosen parameters in turn. However for a direct optimization with k variables, it is very difficult to answer the question why a design works best after the optimization is completed.

C. Optimization algorithm

The bump optimization problem is set up as:

$$\begin{aligned} &\min(C_D(\overrightarrow{DV})) \\ s.t.\quad &\vec{b}_l < \overrightarrow{DV} < \vec{b}_u \end{aligned} \tag{3}$$

where $\overrightarrow{DV}$ is the continuous vector for the free design variables of the bumps, $\overrightarrow{b_l}$ and $\overrightarrow{b_u}$ are their lower and upper bounds, respectively. The drag coefficient C_D is the objective function. During the following optimizations, the lift coefficient C_L will be fixed by the CFD solver by allowing the angle of attack to change. This strategy has eliminated the need to set C_L as a nonlinear constraint and greatly simplify the optimization problem.

It is well known that transonic flow can be very sensitive to the shapes of airfoils or wings and it is possible that the design space of a 2D or 3D bump may have multiple local minima. Hence it makes more sense to search the design space by using an optimizer with the ability of global exploration rather than local exploitation. Furthermore, the numerical simulations based on the RANS equation are very expensive so that the global optimization algorithms assisted by some kind of surrogate models [23, 24] are preferred. Based on the experiences in the previous research [25], a global optimization method known as Efficient Global Optimization (EGO) [26, 27] which can automatically balance the local exploitation and global exploration is adopted here. The Kriging model is used in the EGO algorithm. The comparisons of Kriging-based optimization algorithms with others can also be found in Ref. [36, 37]. To enhance its local search ability, after the EGO search, a local optimizer named BOBQYA developed by Powell [28] is used to further improve the results. The BOBQYA optimizer belongs to the derivative-free optimization algorithm, and it is suited for simulation-based optimization, such as the CFD-based optimization.

III. Results and Discussion

A. Validation of CFD solver

The CFL3D v6.7 solver has been chosen in this study. CFL3D is a long-standing Reynolds-averaged Navier-Stokes CFD code developed at NASA. Recently, its source code has been released publicly under the Apache License, Version 2.0 [35]. This code was thoroughly tested in numerous cases, and a recent validation of the Common Research Model created for the Fifth Drag Prediction Workshop can be found in Ref. [29].

A common baseline airfoil used to study the bumps is the RAE5243 airfoil [9], a natural laminar flow airfoil with a maximum thickness-to-chord ratio of 14%. A test case of RAE5243 airfoil with the data measured in the wind tunnel experiment by Fulker and Simmons [30] is present here for comparison. The flow conditions are M_∞=0.6799, Re_c=18.68×10^6 and the angle of attack α=0.77°. In the experiment, the flow transitions on upper and lower surfaces were both tripped at 5% percent chord. At first, a C-type mesh with 249×65 points shown in Figure 2a was generated and the first cell height above the wall will be adjusted to make sure the y+ value is of O(1) in the viscous sub-layer. To capture the shock wave on the upper surface, the mesh around the shock wave was locally refined. To study the sensitivity of the number of mesh points, a coarser mesh with 125×33 points and two finer meshes with 497×129 and 993×257 points respectively are also generated. Both of the Spalart Allmaras one equation turbulence model (SA) and Menter's SST two equation turbulence model (SST) are adopted in this case. The flow around the airfoil is assumed to be fully turbulent in the numerical calculations.

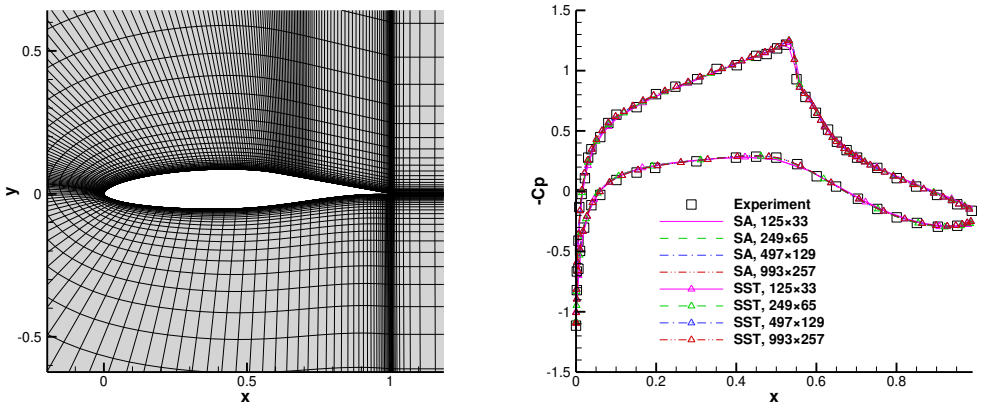

a) Mesh (249×65) b) Pressure coefficient distributions, $C_L=C_{L,experiment}$

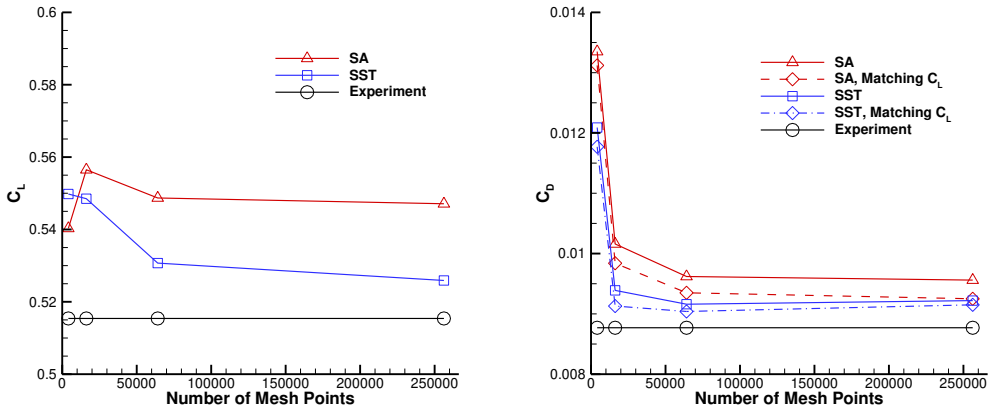

c) Lift coefficients vs Mesh points d) Drag coefficients vs Mesh points

Fig. 2 RAE5243 airfoil, M_∞=0.6799, $Re_c=18.68\times10^6$ and α=0.77°.

Figure 2 shows the comparison of the numerical results and experiment data. Initially the angle of attack in the computation was fixed to be the same as that in the experiment, and it was found that the lift and drag coefficients by the computation are both slightly higher than that of the experiment. Considering the potential wall interference for transonic wind tunnel tests, the strategy of matching the lift coefficient by the experiment was adopted, resulting in a better agreement in drag with the experiment if the lift is matched. As shown in Figure 2, it is clear that the Menter's SST model can give better results. Furthermore, it is also less sensitive to the number of mesh points. Figure 2b shows the comparison of surface pressure coefficient distributions between the experiment and computation. The computational results show a good agreement with the experimental data and the number of mesh points and turbulence model both have little effects on the surface pressure coefficient distribution.

B. Bump optimization

The flow conditions chosen here are the same as the validation case, as shown in the previous section. In order to generate a stronger shock wave to be studied, a high-loading case with C_L=0.82 is considered. The location of the shock wave on the upper surface is around 55% chord. An infinite unswept wing with the section of RAE5243 airfoil is used to accommodate the 2D and 3D bumps. Only half of a 3D bump will be simulated due to the symmetry of the flow field. The total span of the 3D bump is set to be free depending on the bump width.

According to the previous study, the Menter's SST model is adopted here. One study conducted by Mclntosh and Qin [31] shows that the transition location has little effects on the performances of shock control bumps. Therefore the flow around the wing section is assumed to be fully turbulent. The C-type mesh with 497×129 points is adopted for the wing section, and the number of span-wise grid points for a half bump is initially set to be 65. Thus the total number of mesh points is 497×129×65. The machine used to run the simulations is a Dell workstation with 2 Intel Xeon(R) E5-2640 v4 CPUs. The mesh has been divided into 8 blocks for parallel computations. It took about an hour to finished one calculation with converged results.

Since the deformation caused by the bumps is usually small, an algebraic grid deformation technique [25] was employed to update the volume mesh. This simple mesh update method is not only fast but also maintains the original mesh quality, which is very important for optimization to ensure consistency of the results for different designs.

Here the 2D bump optimization with four free design variables and 3D bump optimization with six free design variables were carried out at first. After the optimization, a mesh sensitivity study was also carried out to check the feasibility of the current mesh. The results are presented in Figure 3. It appears that the current mesh with 497×129×65 points is sufficient to meet the requirement of numerical accuracy.

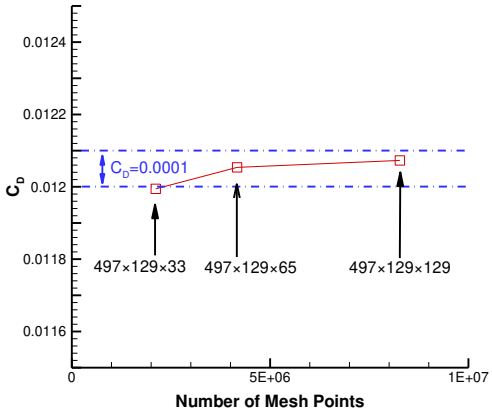

Fig. 3 Mesh sensitivity study for the optimized 3D bump.

Table 1 shows the drag coefficients of the optimized bumps. It can be seen that the drag coefficients of the 2D bump is slightly lower than that of the 3D bump. The difference of the drag reductions is about 0.54%, which is insignificant in comparison to almost one-fifth of the drag savings.

Table 1 Drag coefficients of the 2D and 3D bump optimizations

	RAE5243	2D bump	3D bump
C_D	0.01496	0.01197	0.01205
Drag reduction	-	19.99%	19.45%

Table 2 Optimized parameters of the 2D and 3D bumps

	Bump length	Bump crest	Relative crest	Bump height	Relative bump span	Total span	S_{mc}
Bounds	0.0 - 0.3	0.5 - 0.8	0.3 - 0.9	0 - 0.06	0.0 - 1.0	0.0 - 0.2	-
2D	0.300	0.635	0.615	0.00634	-	-	0.0063
3D	0.300	0.623	0.553	0.01149	1.000	0.104	0.0057

The final optimized parameters are given in Table 2. Note that, in addition to two non-dimensional design variables, relative crest position and relative bump span, the other bump parameters are also non-dimensionalized by the chord length of the wing. Here define the maximum cross-sectional area per unit wing span as

$$S_{mc} = \int_{z=0}^{z=1c} y(x,z)\big|_{x=crest}\, dz \tag{4}$$

where c represents the chord length.

In Table 2, it can be seen that the optimizers tend to drive the bump length and relative bump span to their upper bounds, indicating that longer and wider bump gives better performance in this case. In fact, the surface area per unit wing span covered by bumps only depends on these two parameters. It suggests that in this case more control surface area can bring more benefits for drag reduction. Also it can be derived that S_{mc} of the 3D bump is very close to that of the 2D bump. Since the other parameters except the bump height also have minor differences, as mentioned in Sec. II.A, it can be seen that the cross-sectional area distribution of the 3D bump is approximately equal to that of the 2D bump.

Figure 4 shows the comparison of pressure coefficient distributions and Figure 5 the comparison of Mach contours. In these figures, a 3D wave structure can be observed in the flow field of a 3D bump. At the z=50% plane, where the height is nearly equal to the height of the 2D bump, the pressure coefficient distribution of the 3D bump is almost the same as that of the 2D bump. At the z=0% plane, where the maximum crest is located, in comparison with the 2D bump, the pressure before the crest increases and the pressure after the crest decreases due to higher geometric curvature.

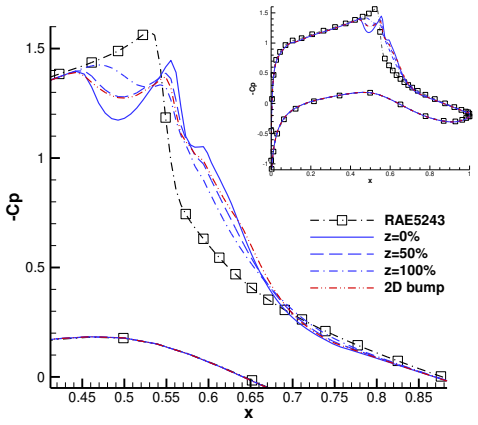

Fig. 4 Comparison of pressure coefficient distributions, "z" represents the relative bump span and z=0% corresponds to the maximum crest of this 3D bump.

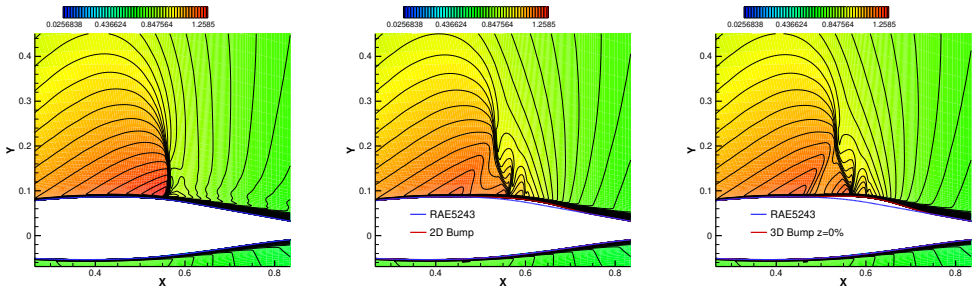

a) RAE5243, M_{peak}=1.309 b) 2D bump, M_{peak}=1.217 c) 3D bump z=0%, M_{peak}=1.227

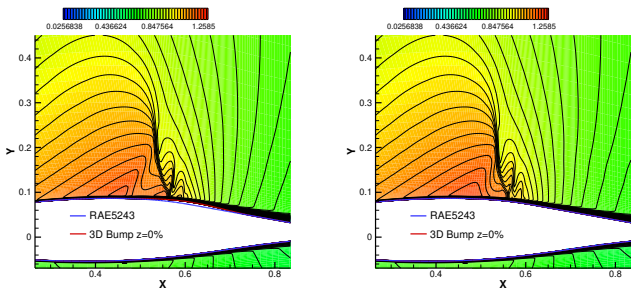

d) 3D bump z=50%, M_{peak}=1.220 e) 3D bump z=100%, M_{peak}=1.229

Fig. 5 Comparison of Mach number contours, "z" represents the relative bump span and z=0% corresponds to the maximum crest of this 3D bump, and "M_{peak}" represents the peak Mach number.

However, the deviation at the z=0% plane are compensated by the deviation at the z=100% plane, where the height of this 3D bump is equal to zero. Thus the average pressure coefficient distribution of the 3D bump is approximately equal to that of the 2D bump. Figure 6 shows the comparison of surface skin friction lines. A tiny shock-induced separation bubble can be observed in Figure 6a. After controlling the shock wave, the separation bubble disappears due to the reduction of the shock wave strength. The S-shaped skin friction lines on the surface of the 3D bump can be clearly seen in Figure 6c, indicating the cross flow caused by the spanwise pressure gradient.

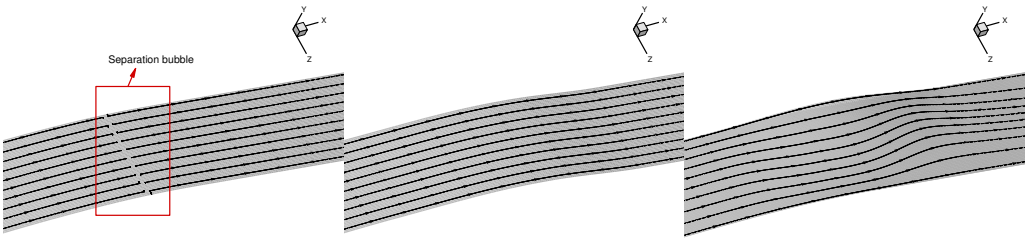

a) RAE5243 b) 2D bump c) 3D bump

Fig. 6 Comparison of skin friction lines on the different wings.

C. Comparison of 2D and 3D bumps and the transonic area rule

For aircraft flying at the transonic region, one of the basic design guidelines is the well-known "transonic area rule" first discovered by Whitcomb [32]. The transonic area rule says that near the speed of sound the wave drag of a low-aspect-ratio thin-wing and body combination is primarily dependent on the axial development of the cross-sectional areas normal to the airstream. This is later generalized as a design requirement for a smooth streamwise variation of total cross-sectional area for an aircraft configuration to avoid substantial compressibility effect and wave drag. In other words, configurations with the same streamwise cross-sectional area variation should have similar compressibility effects. A more detailed description of the transonic area rule can be found in Ref. [33].

In classic aerodynamics, the transonic area rule can be applied in a slender wind-body aerodynamic shape at Mach number around 1 when the viscous effects are insignificant. In this study, it is observed that the principle of the transonic area rule also works quite well on the shock control bumps beneath normal shock waves. Therefore, the transonic area rule helps us to explain the similarity of the behavior of the 2D and 3D bumps. Its validity will be further confirmed by the following studies.

As mentioned before, Qin *et al*. [11] observed from their bump optimization study that the heights of the optimized 3D bumps are approximately two times of that of the optimized 2D bumps. Thus they suggest a "cross-

sectional area hypothesis" [34] that says if the maximum cross-sectional area of the 3D bump is the same as that of the 2D bump, the performances of them will be approximately the same. This hypothesis can actually be related to the transonic area rule. By adopting the view of the area rule, some of the characteristics of 3D bumps can be explained. Although the flow structures of 2D and 3D bumps are not quite the same, their aerodynamic performances can reach a similar level through optimal designs because the wave drag primarily depends on the streamwise cross-sectional area distribution according to the transonic area rule. Unlike 2D bumps, the flow structures around 3D bumps can be affected by their cross-flow components as shown in Fig. 6c.

As shown in Table 2, the 3D bump has a lower S_{mc} at the optimum and this may be explained by the fact that the 3D bump has a much higher crest (almost two times of that of the 2D bump) and strong spanwise surface variation, resulting in a thicker boundary layer and more viscous drag. Therefore the optimizers have led to a smaller area S_{mc} for the 3D bump for optimum.

D. Optimization enhanced parametric study

D-1. Total span

The number of 3D bumps per unit wing span depends on the total span relative to the wing chord, and in this section its effects will be investigated in detail. Since the sensitivities of these design parameters are widely distributed, it is very difficult to find a general principle. Thus the choice of grid sampling points can only rely on experiences based on previous works. The grid sampling points chosen for the total span are 0.0125, 0.025, 0.050, 0.075, 0.100, 0.125, 0.150, 0.175 and 0.200 of the chord length, which correspond to 40, 20, 10, $6\frac{2}{3}$, 5, 4, $3\frac{1}{3}$, $2\frac{6}{7}$ and $2\frac{1}{2}$ bumps per unit wing span, respectively. The other five parameters are set to be free for optimization. The upper and lower bounds are the same as that in Table 2. After the optimizations, it is found that the bump length and relative bump span are both driven to their upper bounds by the optimizers, confirming the findings in the previous section. The other optimized parameters can be found in Figure 7b. It can be seen that the bump crest does not change much since it depends mostly on the location of the shock wave on the upper surface. As the total span increases, the bump height increases slightly and the relative crest moves slightly downstream.

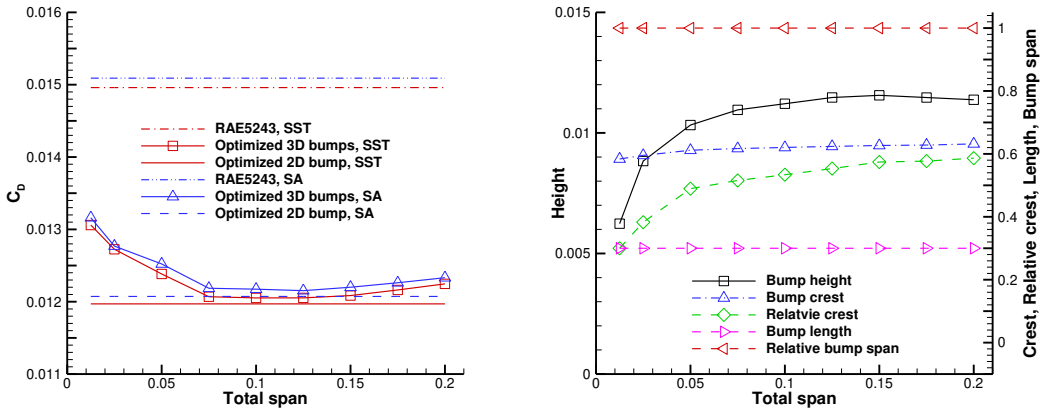

a) Drag coefficients b) Optimized parameters

Fig. 7 Optimized results of 3D bumps with different total spans.

Figure 7a shows the drag coefficients by the optimized bumps with different total span. It can be observed that the landscape of the design space actually has a flat part, which is approximately between 0.075c and 0.15c. The drag coefficients gradually rise as the total span moves away from this flat region. The skin friction lines shown in Figure 8 suggest that the increase of drag is mainly due to flow separation for either a very narrow or very wide 3D bump. To study the effects of the turbulence models, the numerical results based on the SA turbulence model are also presented in Figure 7a and Figure 9. In comparison with the SST turbulence model, these figures show that the SA turbulence model has given slightly higher drag coefficients and larger separation bubbles. However, as shown in Figure 7a, the drag reductions predicted by these two turbulence model are almost the same.

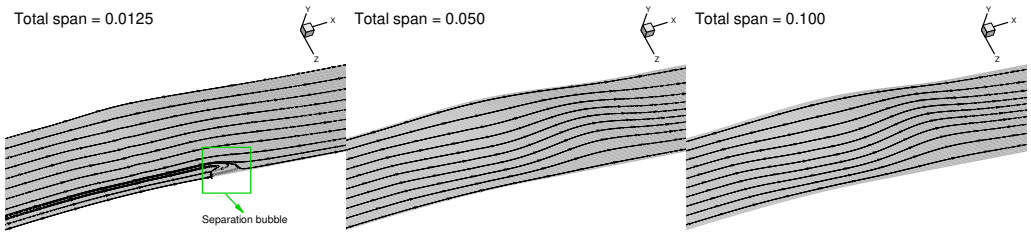

a) *TS* =0.0125 b) *TS* =0.050 c) *TS* =0.100

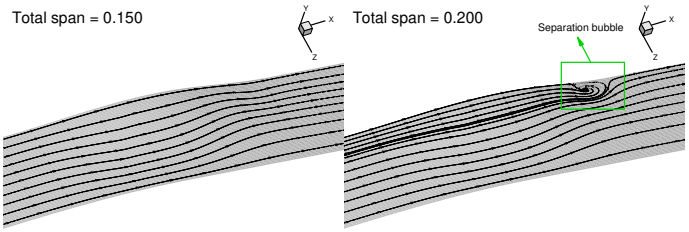

d) *TS* =0.150 e) *TS* =0.200

Fig. 8 Skin friction lines on the surfaces of 3D bumps with different total spans. The wing sections have been scaled in the z-axis direction properly for display purpose. The SA turbulence model has been used.

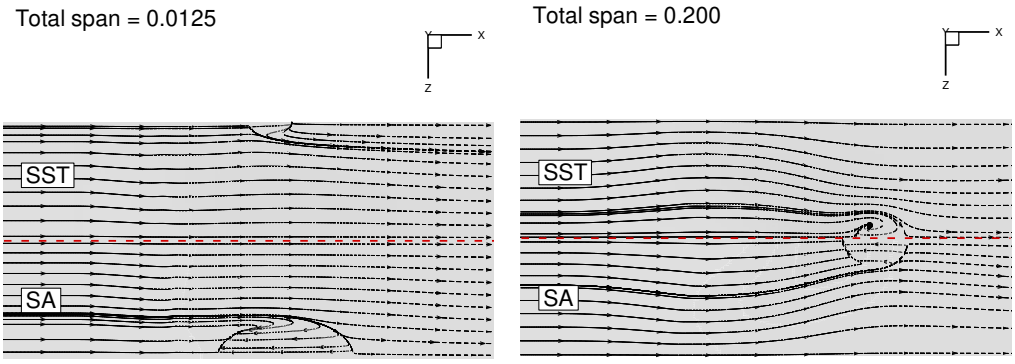

a) *TS* =0.0125 b) *TS* =0.200

Fig. 9 Comparison of skin friction lines using two different turbulence models. The wing sections have been scaled in the z-axis direction properly for display purpose.

Figure 10a compares the maximum cross sectional area of 3D bumps with different total spans. Apparently, if one increases the number of 3D bumps, the local spanwise curvature also increases. When the cross flows on the rear part of 3D bumps encounter the wall surfaces with very high local curvature, the flow separation occurs eventually. If the local curvature is reduced by using wider bumps, the flows become attached as shown in Figure 8. However, if the total span is too large, about half its own length in this case, a relatively wider crest will increase the

streamwise pressure gradient on the rear part of the bump as shown in Figure 10b, causing a flow separation bubble behind the crest.

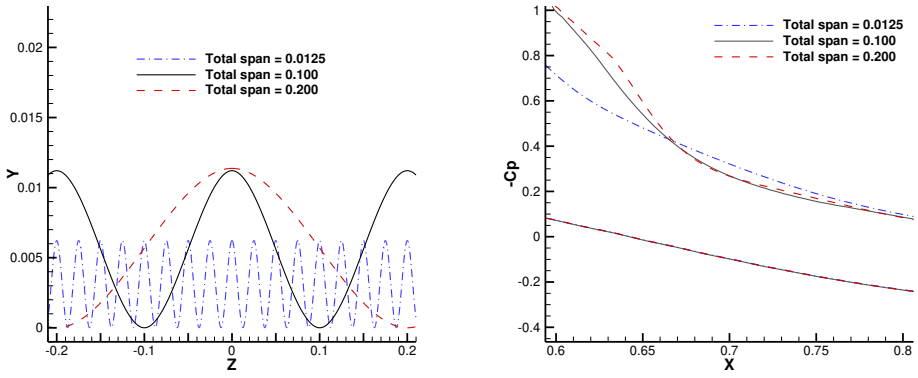

a) Maximum cross sections b) Pressure coefficient distributions at the z=0%

Fig. 10 Comparison of 3D bumps with different total spans.

If the viscous effects are neglected, from the transonic area rule mentioned earlier, the performances of 3D bumps with different total span should be the same, since the cross-sectional area distribution is the same. Simply changing the total span does not change the cross-sectional area distribution in the streamwise direction. However, due to the viscous effects, very small or large span causes flow separation as shown earlier. The optimizer tends to reduce the bump height to mitigate the viscous effects. Figure 7 shows that the variations of the drag coefficient and bump height have opposite trends. This complicated nonlinear behavior can only be identified by studying one specified parameter while the other parameters are kept to be optimal. Hence the benefit of using the optimization enhanced parametric study method is clearly demonstrated.

D-2. Relative bump span

In this section the effects of the relative bump span will be studied. The grid sampling points chosen for the relative bump span are 25%, 50%, 75% and 100%. Here the total span will be fixed as 10%c according to the research above. The other four parameters are set to be free for optimization. The upper and lower bounds are the same as that in Table 2. All of the bump lengths reach the upper bounds, which are 0.30c.

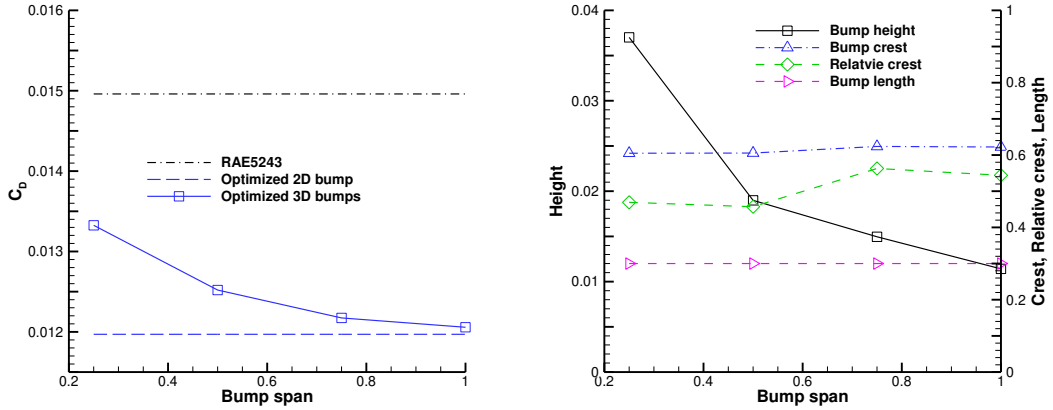

a) Drag coefficients

b) Optimized parameters

Fig. 11 Optimized results of 3D bumps with different relative bump spans.

The optimized results are given in Figure 11. Unlike the total span case, the bump performance steadily improves as the relative bump span increases, indicating larger bump area provide more drag reduction. When the relative bump span is equal to 100%, the drag reduction of this 3D bump reaches to its maximum, which is very close to that of the 2D bump. Figure 12 shows the maximum cross sectional area in the y-z plane. Apparently, the maximum cross-sectional area still plays a key role on the bump performance. However, the area rule does not strictly hold true here, although the bump height does increase as the relative bump span shrinks. The reason lies in the fact that a higher bump causes more viscous drag, moderating the total drag reduction. Figure 13 shows the skin friction lines on the surfaces of these 3D bumps. It is obvious that the flow separation takes place as the bump becomes too high and the high local curvature is responsible for it.

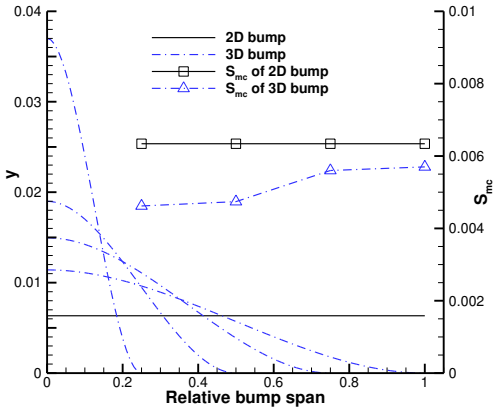

Fig. 12 Maximum cross sections of 3D bumps with different relative bump spans.

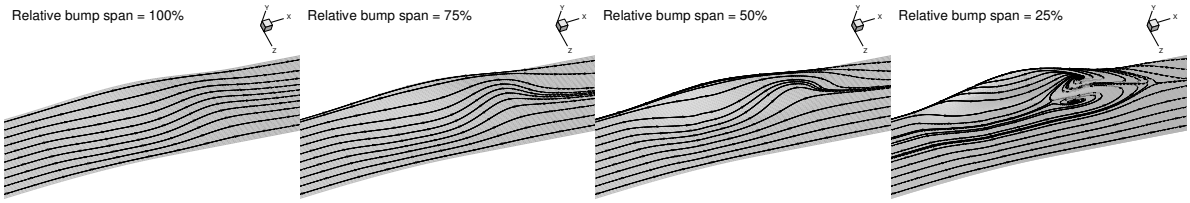

a) *RS* =100% b) *RS* =75% c) *RS* =50% d) *RS* =25%

Fig. 13 Skin friction lines on the surfaces of 3D bumps with different relative bump spans

In fact, two different flow mechanisms which drive the optimizers to different directions can be easily identified. The first one is the inviscid flow mechanism which can be explained by the area rule, the maximum cross-sectional area tends to be close to that of the 2D bump and therefore the bump tends to be higher to reduce the wave drag as it becomes narrower. But if the bumps become too high, flow separation occurs, leading to more viscous drag. The optimizer attempts then to lower the bump height to mitigate the detrimental effects. Finally, a compromise is found by the optimizer. This is the reason why the maximum cross-sectional areas of the optimized 3D bumps are slightly smaller than that of the optimized 2D bump.

Eastwood and Jarrett [18] made a comparison of the performances of 2D and 3D bumps by using the parametric study method, leading to the conclusion that the on-design performance of the 3D bump is worse than that of the 2D bump. However, since the heights of both 2D and 3D bumps were fixed to the same value in their study, the potential of the 3D bump was underestimated. They also introduced a design parameter called the isolation ratio to describe the size of clean wing area. They found that as the isolation ratio decreased while the height was kept to be the same value, the lift-to-drag ratio increased. When the isolation ratio was equal to zero, the 3D bump became a 2D bump (assuming there were no shoulder sections for simplicity). Thus in their study the 2D bump was the limiting case of 3D bumps. The 3D bump in their study can be simply seen as a finite 2D bump plus two shoulder sections and therefore decreasing the isolation ratio is roughly equivalent to increasing the span size of this finite 2D bump. Note that as the isolation ratio decreases, their 3D bump cross-sectional area increases, affecting the performance due to the transonic area rule. Unlike their study, when the height is treated as a design variable, as shown in Figure 12, a pure 3D bump is always maintained in the current research. The reason why the 3D bump can compete with the 2D bump is because of the almost identical cross-section area distribution, and is not because the geometry of the 3D bump becomes more like a 2D bump.

D-3. Bump length

The previous sections have shown that longer bumps have better performance. The effects of the bump length will be studied here in more detail. The grid sampling points chosen for the bump length are 0.1, 0.2, 0.3, 0.4 and 0.5 of the chord length. The other parameters are set to be free for optimization. The upper and lower bounds are the same as that in Table 2. The drag coefficients of the optimized bumps are shown in Figure 14a. It is obvious that longer bumps provide more drag savings and the performances of the 2D and 3D bumps are nearly the same.

Figure 14b shows the final optimized design variables. It can be seen that two streamwise parameters, bump crest and relative crest, of the 2D and 3D bumps are very close to each other. The heights of the 3D bumps are almost two times that of the 2D bumps, which means that their maximum cross-sectional areas are almost the same based on the way that the 3D bump is defined. This suggests that the transonic area rule still holds true for bumps with different length. As shown in Figure 15, as the bump length increases, the maximum cross-sectional area also increases.

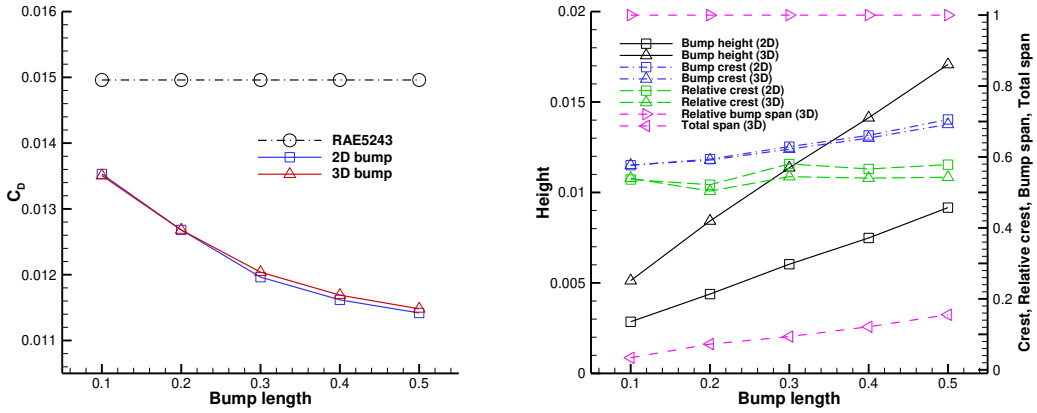

a) Drag coefficients b) Optimized parameters

Fig. 14 Optimized results of 2D and 3D bumps with different lengths

A key parameter derived from the relative crest and the bump average height is the bump incident angle, which is defined as

$$\theta = \arctan\left(\frac{h_{avg}}{len \times c_{relatvie}}\right) \tag{5}$$

where *len* is the bump length, $c_{relative}$ is the relative crest, and h_{avg} is the average bump height. For a 2D bump, h_{avg} is equal to its maximum height, and for a 3D bump, h_{avg} is equal to S_{mc} divided by the unit wing span.

The bump incident angle is one of the major factors influencing the compression waves or the front leg of the λ shock. Figure 15 shows the bump incident angles of the 2D and 3D bumps. It is interesting to note that both the bump incident angles of the 2D and 3D bumps vary slightly tending from 3° to 2° as the bump lengths increases, indicating the importance of this parameter in the physical process of weakening the shock wave.

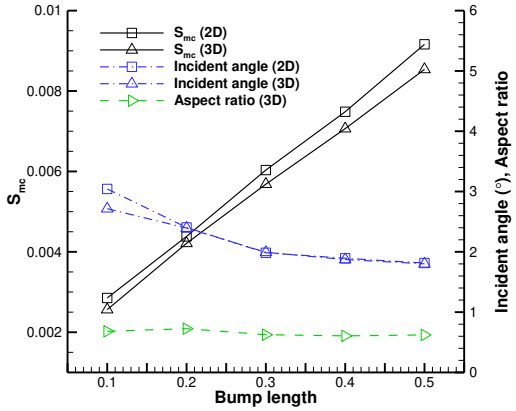

Fig. 15 Optimized parameters of 2D and 3D bumps with different lengths

Figure 14b also shows that as the bump length increases, the bump width increases, suggesting that the length and width of the 3D bumps should be related to each other. As shown in Figure 15, the best 3D bump aspect ratio is around 0.67 or 2/3. As discussed earlier, wider or narrower 3D bump can cause flow separation, bringing in drag penalty.

D-4. Mach number

It is well known that the optimized bump parameters are highly sensitive to the strength and location of the shock wave, so it is worthwhile to check the effects of the free-stream Mach numbers on the optimized bump performance. Since RAE5243 airfoil has a 14% maximum thickness and its design Mach number is around 0.7, the grid sampling points chosen for free stream Mach number are 0.70, 0.71, 0.72, 0.73 and 0.74. The value of C_L has been set to 0.45 for a cruise case. According to the study above, the bump length and relative bump span are fixed as 0.3c and 100%, respectively. Thus, for the 2D and 3D bumps, the number of free design variables has been reduced to be 3 and 4, respectively. The upper and lower bounds for the free parameters are the same as that in Table 2.

Figure 16 shows the optimized results at different Mach numbers. It can be seen in Figure 16a that both 2D and 3D bumps can lower the drag coefficient hugely if their control parameters are at their optima. The drag coefficients of 3D bumps are slightly higher than that of 2D bumps, and the difference gradually increases as the Mach number increases. This is believed to be due to the viscous effect becoming more serious as the height of the 3D bump

increases as shown in Figure 16b. However, the differences are trivial in comparison to the huge drag savings at the high speeds. It is also noted that the optimal bump height increases linearly with the Mach number for both 2D and 3D bumps, and the height of the 3D bump is about double that of the 2D one.

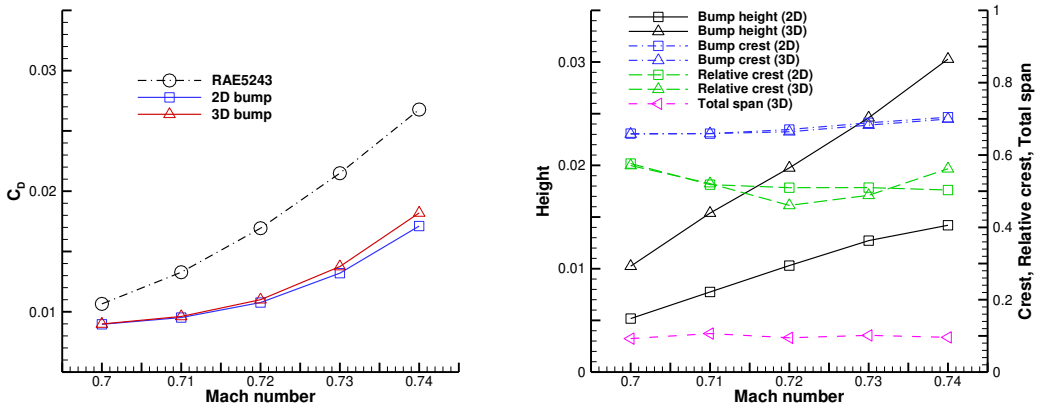

a) Drag coefficients

b) Optimized parameters

Fig. 16 Optimized results at different Mach numbers.

Figure 17 shows the optimized parameters. It can be seen that the maximum cross-sectional area and incident angle of 2D and 3D bumps increases linearly with the Mach number when it is below 0.73. It is interesting to note that the best aspect ratio of 3D bumps remains around 0.67 or 2/3 for the whole Mach number range studied. These may provide useful design guide for the adaptive bumps needed to operate at different flight speeds.

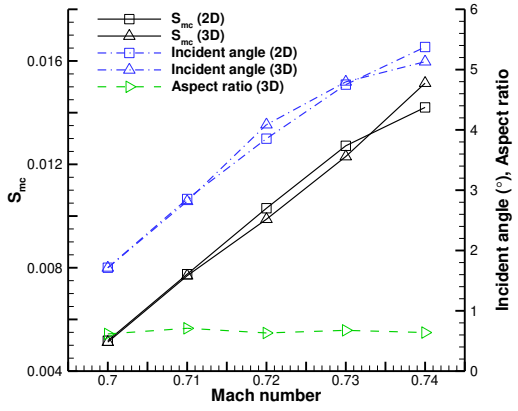

Fig. 17 Optimized parameters of 2D and 3D bumps at different Mach numbers.

Figure 18 shows the comparison of Mach number contours. Unlike a supercritical wing, a natural laminar flow wing has a more convex upper surface which tends to fix the shock position. Hence the location of the shock wave does not change much as Mach number increases, nor does the bump crest as shown in Figure 16b. As the Mach number increases, the wave patterns controlled by the bumps gradually change from a knee-shaped shock waves to a λ-structured shock wave. The knee-shaped shock wave structure was first reported in Ref. [11] from their

optimized bumps, which are clearly shown for the lower Mach cases here. This structure is related to turning the original shock to compression waves ahead of the bump crest. For high Mach numbers, the λ-structured shock waves becomes unavoidable, indicating that it is harder to replace a stronger shock wave with compression waves. The same trends can be clearly observed from both the optimized 2D and 3D bumps.

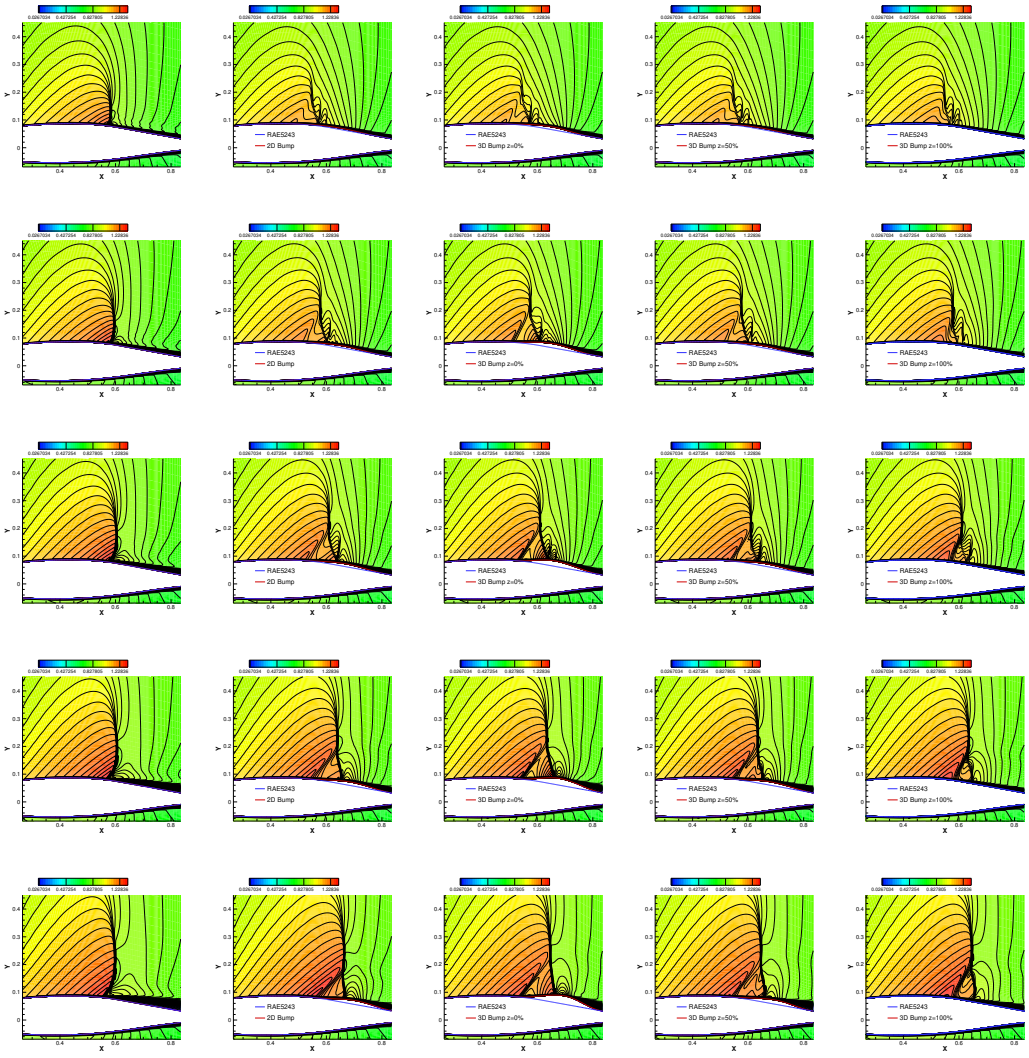

Fig. 18 Comparison of Mach number contours. The columns from left to right correspond to RAE5243 airfoil, optimized 2D bump, and optimized 3D bump at z=0%, 50% and 100% span, respectively. The rows from top to bottom correspond to Mach=0.70, 0.71, 0.72, 0.73 and 0.74, respectively.

IV. Conclusion

A parametric study method assisted by optimizations has been developed to explore the design spaces of the 2D and 3D shock control bumps. This study shows that this parametric study method could provide much more useful information about the problem to be studied in exploring the design space. As it has been demonstrated in this paper,

that there is strong interaction among design parameters for 2D and 3D bumps. By studying one specific parameter while the other parameters are at their optima, the interactive effects have been properly investigated, and some of the distinct flow features induced by shock control bumps have been revealed.

From the present study, it has been found that the 2D and 3D shock control bumps have nearly the same performance through optimal designs, although the flow physics of 2D and 3D bumps are rather different. This can be partially explained by the transonic area rule since the optimized 2D and 3D bumps have almost identical streamwise cross-sectional area distribution.

A key design parameter for the 2D and 3D bumps is the maximum cross-sectional area. To match the performance of a 2D bump, a 3D bump should match the 2D maximum cross-sectional area. Therefore the height and width of 3D bumps should be treated as a whole to be designed. However, caution needs to be exercised before applying this principle directly, since it can be affected by stronger viscous effects for the 3D bump.

It has been found that the incident angle of an optimized bump does not change significantly with varying bump design length at the same Mach number and furthermore it has an approximate linear relation with the Mach number.

For 3D bumps, the bump aspect ratio has been found to be an important parameter. From the present study, the best aspect ratio is around 0.67 or 2/3, no matter what the bump length or the shock strength is. A too narrow 3D bump causes flow separation on the sides of the bump between two bumps, and a too wide 3D bump induces a separation bubble behind the bump crest. Both types of separation degrade the bump performance. Thus, after the bump length is decided, the bump width has to be chosen carefully to avoid these detrimental effects.

Acknowledgments

This work was funded by the project 11502112, 11432007 and 11672132 supported by National Natural Science Foundation of China. This work was also supported by the Fundamental Research Funds for the Central Universities No.NS2014013 and a project funded by the Priority Academic Program Development of Jiangsu Higher Education Institutions of China. The first author would also like to thank the funding from University of Sheffield pump priming research funds to support his research stay at the University of Sheffield.

References

[1] Tai TC. Theoretical Aspects of Dromedaryfoil. David W. Taylor Naval Ship Research and Development Center, Tech. Report no. 770104, Nov 1977.

[2] Tai TC, Huson GG, Hicks RM and Gregorek GM. Transonic Characteristics of a Humped Airfoil. *Journal of Aircraft* 1988; 25: 673–674.
doi: 10.2514/3.45642

[3] Ashill P, Fulkner J and Shires A. A Novel Technique for Controlling Shock Strength of Laminar-Flow Aerofoil Sections. *DGLR Bericht*, Pt. 6, 1992, pp. 175–183.

[4] Fulker JL, Ashill PR and Simmons MJ. Study of Simulated Active Control of Shock Waves on an Aerofoil. Defence Research Agency, Technical. Rept. TR93025, May 1993. Farnborough: Defence Research Agency.

[5] Stanewsky E, Délery J, Fulker J and Geißler W. Synopsis of the Project EUROSHOCK. *Notes on Numerical Fluid Mechanics: EUROSHOCK - Drag Reduction by Passive Shock Control, Results of the Project EUROSHOCK*, Vol. 56, Friedr. Vieweg & Sohn Verlagsgesellschaft mbH, Braunschweig/Wiesbaden, 1997, pp. 1–81.

[6] Birkemeyer J, Rosemann H and Stanewsky E. Shock Control on a Swept Wing. *Aerospace Science and Technology* 2000; 4: 147–156.
doi: 10.1016/S1270-9638(00)00128-0

[7] Stanewsky E. Adaptive Wing and Flow Control Technology. *Progress in Aerospace Sciences* 2001; 37: 583–667.
doi: 10.1016/S0376-0421(01)00017-3

[8] Stanewsky E, Délery J, Fulkner J and De Matteis P. Synopsis of the Project EUROSHOCK II. *Notes on Numerical Fluid Mechanics and Multidisciplinary Design: Drag Reduction by Shock and Boundary Layer Control—Results of the Project EUROSHOCK II*, Vol. 80, Springer-Verlag Berlin Heidelberg, 2002, pp. 1–124.

[9] Qin N, Zhu Y and Shaw ST. Numerical Study of Active Shock Control for Transonic Aerodynamics. *International Journal of Numerical Methods for Heat & Fluid Flow* 2004; 14: 444–466.
doi: 10.1108/09615530410532240

[10] Qin N, Monet D and Shaw ST. 3D Bumps for Transonic Wing Shock Control and Drag Reduction. In: *CEAS Aerospace Aerodynamics Research Conference*, Cambridge, UK, 2002.

[11] Qin N, Wong WS and and Le Moigne A. Three-Dimensional Contour Bumps for Transonic Wing Drag Reduction. *Proceedings of the Institution of Mechanical Engineers, Part G: Journal of Aerospace Engineering.* 2008; 222: 619–629.
doi: 10.1243/09544100JAERO333

[12] Wong WS, Le Moigne A and Qin N. Parallel Adjoint-based Optimisation of a Blended Wing Body Aircraft with Shock Control Bumps. *The Aeronautical Journal* 2007; 111: 165–174.

doi: 10.2514/6.2007-57

[13] Wong WS, Qin N, Sellars N, Holden H and Babinsky H. A Combined Experimental and Numerical Study of Flow Structures over Three-Dimensional Shock Control Bumps. *Aerospace Science and Technology* 2008; 12: 436–447.

doi: 10.1016/j.ast.2007.10.011

[14] Holden HA and Babinsky H. Shock/Boundary Layer Interaction Control Using 3D Devices. In: The 41st Aerospace Sciences Meeting and Exhibit, Reno, Nevada, 2003, AIAA Paper 2003-447.

[15] Ogawa H, Babinsky H, Pätzold M and Lutz T. Shock-Wave/Boundary-Layer Interaction Control Using Three-Dimensional Bumps for Transonic Wings. *AIAA Journal* 2008; 46: 1442–1452.

doi: 10.2514/1.32049

[16] Bruce PJK, Colliss SP and Babinsky H. Three-dimensional shock control bumps: effects of geometry. In: 52nd Aerospace Sciences Meeting, National Harbor, Maryland, 2014, AIAA 2014-0943.

[17] Colliss SP, Babinsky H, Nübler K and Lutz T. Vortical Structures on Three-Dimensional Shock Control Bumps. *AIAA Journal* 2016; 54: 2338–2350.

doi: 10.2514/1.J054669

[18] Eastwood JP and Jarrett JP. Toward Designing with Three-Dimensional Bumps for Lift/Drag Improvement and Buffet Alleviation. *AIAA Journal* 2012; 50: 2882–2898.

doi: 10.2514/1.J051740

[19] Jones NR, Eastwood JP and Jarrett JP. Adapting Three-Dimensional Shock Control Bumps for Swept Flows. *AIAA Journal* 2017; 55: 861-873.

doi: 10.2514/1.J055169

[20] Hinchliffe B and Qin N. Using Surface Sensitivity from Mesh Adjoint for Transonic Wing Drag Reduction. *AIAA Journal* 2017; 55: 818-831.

doi: 10.2514/1.J055319

[21] Bruce PJK and Colliss SP. Review of Research into Shock Control Bumps. *Shock Waves* 2015; 25: 451–471.

doi: 10.1007/s00193-014-0533-4

[22] König B, Pätzold M, Lutz T, Krämer E, Rosemann H, Richter K and Uhlemann H. Numerical and Experimental Validation of Three-Dimensional Shock Control Bumps. *Journal of Aircraft* 2009; 46: 675–682.

doi: 10.2514/1.41441

[23] Sacks J, Welch WJ, Mitchell TJ and Wynn HP. Design and Analysis of Computer Experiments. *Statistical Science* 1989; 4: 409–423.

doi: 10.1214/ss/1177012413

[24] Simpson TW, Poplinski JD, Koch PN and Allen JK. Metamodels for Computer-based Engineering Design: Survey and Recommendations. *Engineering with Computers* 2001; 17: 129–150.
doi: 10.1007/PL00007198

[25] Deng F, Qin N, Liu XQ, Yu XQ and Zhao N. Shock Control Bump Optimization for a Low Sweep Supercritical Wing. *Science China Technological Sciences* 2013; 56: 2385–2390.
doi: 10.1007/s11431-013-5345-8

[26] Jones DR, Schonlau M and Welch WJ. Efficient Global Optimization of Expensive Black-Box Functions. *Journal of Global Optimization* 1998; 13: 455–492.
doi: 10.1023/A:1008306431147

[27] Jones DR. A Taxonomy of Global Optimization Methods Based on Response Surfaces. *Journal of Global Optimization* 2001; 21: 345–383.
doi: 10.1023/A:1012771025575

[28] Powell MJD. The BOBYQA Algorithm for Bound Constrained Optimization without Derivatives. Centre for Mathematical Sciences. Rept. DAMTP 2009/NA06, University of Cambridge, UK, Aug. 2009.

[29] Sclafani AJ, DeHaan MA, Vassberg JC, Rumsey CL and Pulliam TH. Drag Prediction for the Common Research Model Using CFL3D and OVERFLOW. *Journal of Aircraft* 2014; 51: 1101-1117.
doi: 10.2514/1.C032571

[30] Fulker JL and Simmons MJ. An Experimental Study of Shock Control Methods. DRA/AS/HWA/TR94007/1, 1994.

[31] Mclntosh SC and Qin N. The Influence of Transition Onset Location on the Performance of Shock Control Bumps. *Aeronautical Journal* 2013; 117: 1037-1051.
doi: 10.1017/S0001924000008678

[32] Whitcomb RT. A Study of the Zero-Lift Drag-Rise Characteristics of Wing-Body Combinations near the Speed of Sound. National Advisory Committee for Aeronautics, Rept. NACA Technical 1273, 1956.

[33] Carlsen WD. Development of Transonic Area-Rule Methodology. *Journal of Aircraft* 1995; 32: 1056–1061.
doi: 10.2514/3.46836

[34] Wong WS. Mechanisms and Optimizations of 3D Shock Control Bumps. PhD Thesis. University of Sheffield, UK, 2006.

[35] Website: https://cfl3d.larc.nasa.gov/.

[36] Laurenceau J, Meaux M, Montagnac M and Sagaut P. Comparison of Gradient-Based and Gradient-Enhanced Response-Surface-Based Optimizers. *AIAA Journal* 2010; 48: 981-994.

[37]Epstein B, Jameson A, Peigin S, Roman D, Harrison N, Vassberg J. Comparative Study of Three-Dimensional Wing Drag Minimization by Different Optimization Techniques. *Journal of Aircraft* 2009; 46: 526–541.